Comparisons of Rain Rate and Reflectivity Factor Derived from the TRMM Precipitation Radar and the WSR-88D over the Melbourne, Florida, Site

LIANG LIAO

Caelum Research Corporation, Rockville, Maryland

ROBERT MENEGHINI

NASA Goddard Space Flight Center, Greenbelt, Maryland

TOSHIO IGUCHI

Applied Research and Standards Division, Communications Research Laboratory, Tokyo, Japan

(Manuscript received 13 December 2000, in final form 9 May 2001)

ABSTRACT

Validating the results from the spaceborne Tropical Rainfall Measuring Mission (TRMM) precipitation radar (PR) requires comparisons with well-calibrated ground-based radar measurements. At altitudes near the storm top, where effects of PR signal attenuation are small, the data are used to check the relative calibration accuracy of the radars. Near the surface, where attenuation effects at the PR frequency of 13.8 GHz can be significant, the data provide an assessment of the performance of the PR attenuation correction algorithm. The ground-based data are taken from the Doppler Weather Surveillance (WSR-88D) radar located at Melbourne, Florida. In 1998, 24 overpasses of the TRMM satellite over the Melbourne site occurred during times when significant precipitation was present in the overlap region of the PR and WSR-88D. Resampling the ground-based and spaceborne datasets to a common grid provides a means by which the radar reflectivity factors (dBZ) can be compared at different heights and for different rain types over ocean and land. The results from 1998 show that the dBZ fields derived from the PR data after attenuation correction agree to within about 1 dB of those obtained from the WSR-88D with relatively minor variations (0.3 dB) in this difference with height. Comparisons of rain rates also yield good agreement with the conditional mean rain rate from the PR and WSR-88D of 8.5 and 7.6 mm h^{-1}, respectively. The agreement improves in the comparison of area-averaged rain rates where the PR and WSR-88D yield values of 1.25 and 1.21 mm h^{-1}, respectively, with a correlation coefficient for the 24 overpasses of 0.95.

1. Introduction

The precipitation radar (PR) aboard the Tropical Rain fall Measuring Mission (TRMM) satellite is the first weather radar to be flown in space (Simpson et al. 1996; Kummerow et al. 1998; Kozu et al. 2001). Among the questions being addressed in a number of ongoing studies are the accuracy and stability of the PR calibration and the performance of the attenuation correction and rain-rate estimation algorithms.

A variety of approaches can be used to address the calibration issue. Over the three years of PR operation aboard TRMM, satellite instrument data have been used to assess the stability of the transmitter and receiver (Kawanishi et al. 2000). In addition to internal calibration, measurements using an active radar calibrator have been used to monitor the stability of the full system including the antenna characteristics (Kumagai et al. 1995). Space–time averages of the scattering cross sections of the ocean at nadir also provide a check against the same quantity derived from the Ocean Topography Experiment (TOPEX) altimeter. Comparisons between surface cross sections from aircraft radar and the PR have also been reported (Kozu et al. 2001).

Perhaps the most important type of external calibration consists in comparing PR-derived radar reflectivities with the estimates of the same quantity made with well-calibrated ground-based radars (Anagnostou et al. 2001; Schumacher and Houze 2000). However, because of the narrow swath of the PR (215 km), overpasses during rain events at ground-based radar sites are infrequent. Moreover, matching the resolution volumes in space and time from the PR and ground validation (GV) datasets introduces uncertainties. Biases and instabilities in the calibration of some ground-based radars and non-Rayleigh scattering effects at the PR frequency further

Corresponding author address: Dr. Robert Meneghini, Code 975, NASA/Goddard Space Flight Center, Greenbelt, MD 20771.
E-mail: bob@priam.gsfc.nasa.gov

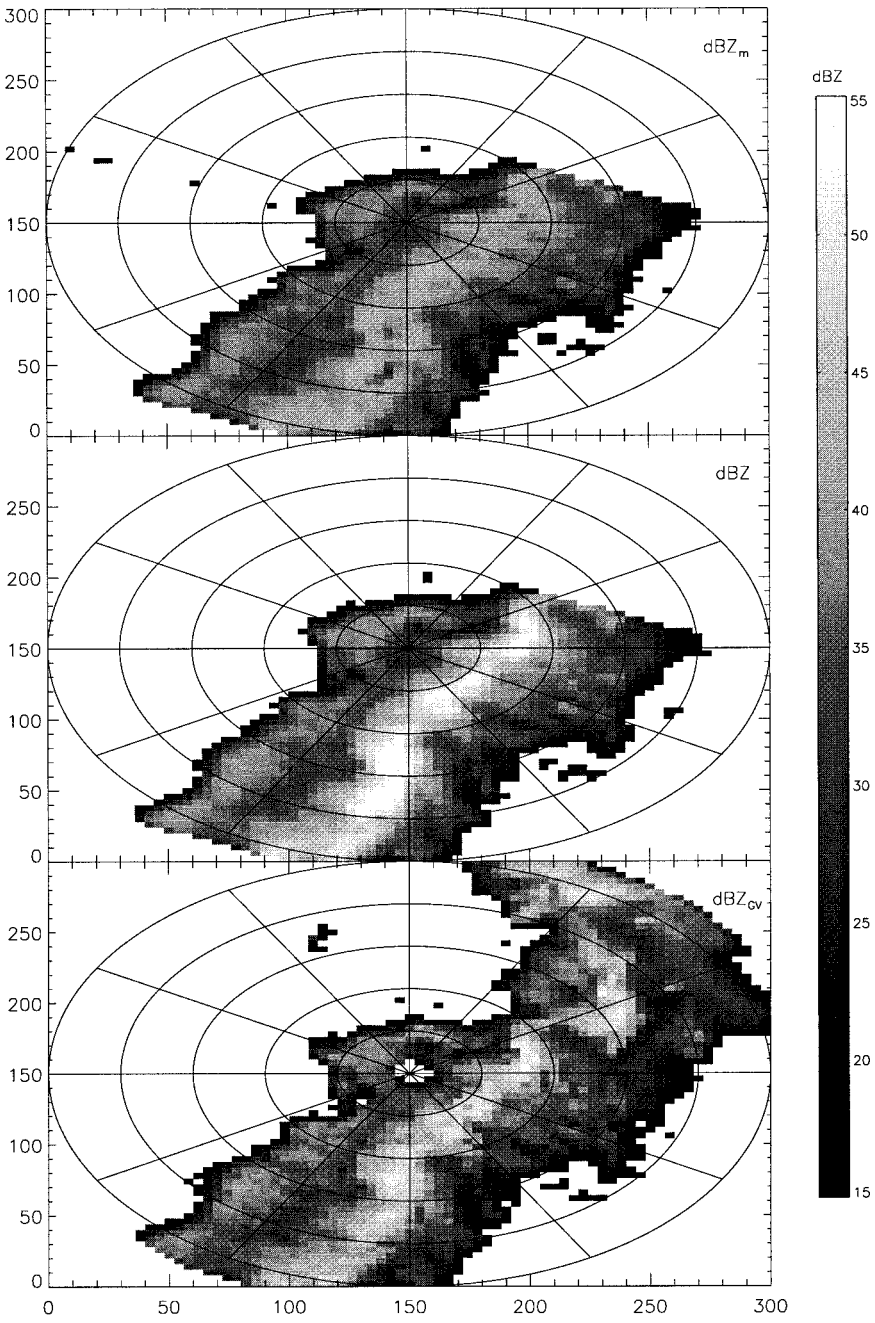

FIG. 1. Maps of radar reflectivities for the 9 Mar 1998 overpass at a height of 3 km. (top) Radar reflectivities from the PR, without attenuation correction. (middle) PR radar reflectivities with attenuation correction. (bottom) Radar reflectivities from the WSR-88D.

TABLE 1. Mean difference Δ of the radar reflectivity factors at 13.8 GHz when the radar reflectivity factor at 3 GHz exceeds 10, 30, and 35 dBZ. Results are given for spherical and oblate raindrops at a temperature of 10°C; for oblates, the ground-based radar is taken to be either horizontally (H) or vertically (V) polarized.

	Sphere			Oblate (H)			Oblate (V)		
dBZ(3 GHz)≥	10	30	35	10	30	35	10	30	35
<dBZ(3 GHZ)>	22.646	34.470	38.733	22.833	34.638	38.820	22.300	34.142	38.566
Δ (dBZ)	0.042	0.767	1.301	0.075	0.797	1.343	0.750	2.048	2.932
Points	18 197	3309	1125	18 258	3490	1256	18 060	2985	910

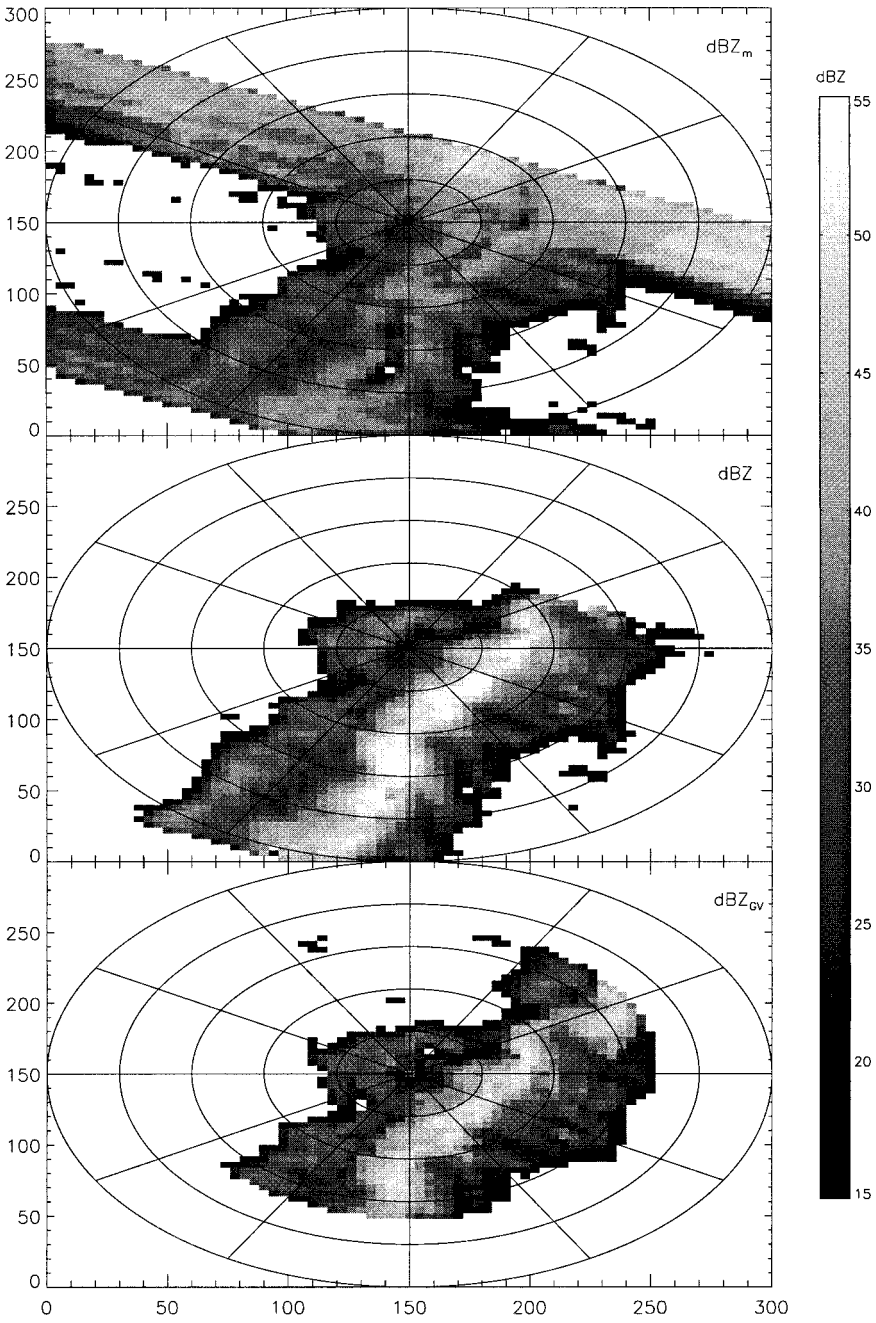

FIG. 2. Same as Fig. 1 except at a height of 1.5 km.

compound the problem. Despite these drawbacks, comparisons with ground-based radars constitute a critical component in testing the accuracy of the PR estimates of radar reflectivity, attenuation, and rain rate.

The focus of the present paper is on comparisons of the coincident PR and GV data over the Melbourne, Florida, site of the Doppler Weather Surveillance (WSR-88D). During 1998, approximately 20 such overpasses occurred in which rain was present in a significant portion of the overlap region. To check how well the detailed images of the dBZ fields match, both sets of radar data are resampled to a 4 km $\times$ 4 km $\times$ 1.5 km grid. Once this is done, the dBZ fields at high altitudes can be used to check the relative calibration accuracy of the two radars, while the radar reflectivity data at altitudes near the surface can be used to assess the performance of the PR attenuation correction algorithm.

By concentrating on the radar reflectivity factor Z, rather than rain rate R, issues of calibration and atten-

TABLE 2. Mean radar reflectivity factors of the WSR-88D (dBZ_{GV}) and the PR with (dBZ) and without (dBZ_m) attenuation correction for the 24 overpass cases at a height of 6 km.

Date	Mean			Correlation		Points
	$\langle dBZ_m \rangle$	$\langle dBZ \rangle$	$\langle dBZ_{GV} \rangle$	dBZ_m–dBZ_{GV}	dBZ–dBZ_{GV}	(N_i)
24 Jan 1998	22.13	22.37	21.93	0.85	0.86	364
17 Feb 1998	23.5	23.61	21.78	0.83	0.83	1807
9 Mar 1998	24.91	25.1	23.04	0.86	0.86	2054
18 Mar 1998	19.27	19.38	17.78	0.79	0.83	82
30 Apr 1998	*****	*****	*****	*****	*****	0
4 May 1998	21.91	21.97	21.19	0.83	0.85	1342
6 Jul 1998	31.86	33.63	31.38	0.75	0.79	157
8 Jul 1998	24.58	25.37	27.63	0.72	0.76	85
10 Jul 1998	21.96	22.09	23.03	0.64	0.66	355
13 Jul 1998	22.08	22.4	25.14	0.82	0.81	517
15 Jul 1998	20.3	20.39	22.81	0.64	0.66	221
18 Jul 1998	27.13	28.08	26.6	0.67	0.66	77
22 Jul 1998	25.35	25.79	24.72	0.59	0.61	82
2 Aug 1998	23.09	23.63	23.74	0.77	0.79	176
4 Aug 1998	22.28	22.55	21.49	0.82	0.83	220
5 Aug 1998	22.5	22.72	23.2	0.75	0.77	512
9 Aug 1998	23.89	24.64	24.48	0.86	0.86	270
15 Aug 1998	28.13	29.69	28.43	0.85	0.86	191
20 Aug 1998	25.55	25.93	25.24	0.81	0.82	674
22 Aug 1998	21.3	21.58	22.07	0.79	0.81	457
18 Sep 1998	22.19	22.46	23.2	0.73	0.74	583
25 Sep 1998	24.86	25.41	25.77	0.76	0.77	236
18 Oct 1998	*****	*****	*****	*****	*****	0
5 Nov 1998	19.25	19.17	17.13	0.52	0.54	1055
Total	23.1	23.34	22.55	0.80	0.82	11 517

uation correction can be separated from those related to the particle drop size distribution (DSD) used in converting Z to R. Nevertheless, the ultimate goal of the validation is to determine the accuracy of the PR-derived rain rates. This is discussed in the final section of the paper where rain rates from the PR and GV are compared over the 4 km $\times$ 4 km $\times$ 1.5 km grid as well as on an area-average basis.

We begin with a brief discussion of the general characteristics of the two datasets and the choice of the grid onto which the PR and GV data are resampled. This is followed by a case study in which scatterplots of the dBZ fields from the PR and GV are shown for several altitudes. Statistics of the rain rates from the GV and PR are presented by scatterplots and histograms of the gridded data as well as on the basis of instantaneous area averages. Divisions of the data into stratiform and convective classes show that the area-averaged rain rates are in good agreement despite the different rain classification schemes and Z–R relationships that are used.

2. Resampling PR and GV data to a common grid

The basic PR volume element is 0.25 km in the range direction and approximately 4 km $\times$ 4 km in the transverse plane. Since the cross-track PR scan is confined to near-nadir incidence angles ($<18°$), the range direction is approximately vertically directed and the transverse plane is approximately horizontal. The GV quantities are taken from the standard data products 2a-55 (dBZ) and 2a-53 (R) that are defined over a resolution cell of 2 km $\times$ 2 km in the horizontal and 1.5 km in the vertical (http://trmm.gsfc.nasa.gov). It should be noted that the standard TRMM Science Data and Information System (TSDIS) product gives rain rates only at the lowest vertical level from the surface to 1.5 km.

In this study we take the common resolution cell to be a volume of 4 km $\times$ 4 km in the horizontal and 1.5 km in the vertical. The PR-derived dBZ at the center of each element is found by the following procedure.

1) Convert dBZ to Z.
2) Resample the Z data onto horizontal planes spaced 250 m apart.
3) For the data on each plane, perform a Delaunay triangulation and interpolation to a 4 km $\times$ 4 km grid. We have done this using the interactive data language (IDL) routine ''TRIANGULATION.''
4) Average the interpolated data on each plane over 1.5 km vertical extent so that the data are specified on a 4 km $\times$ 4 km $\times$ 1.5 km grid.
5) Convert Z to dBZ.

It is important to note that the interpolation is done linearly in Z so that the dBZ values read from the output of PR algorithm 2a-25 are converted to Z, resampled onto the common grid, and then converted back to dBZ. As the rain rate R is obtained directly from 2a-25, conversions from decibels to linear scale are not required. A similar procedure is used to resample the dBZ and R

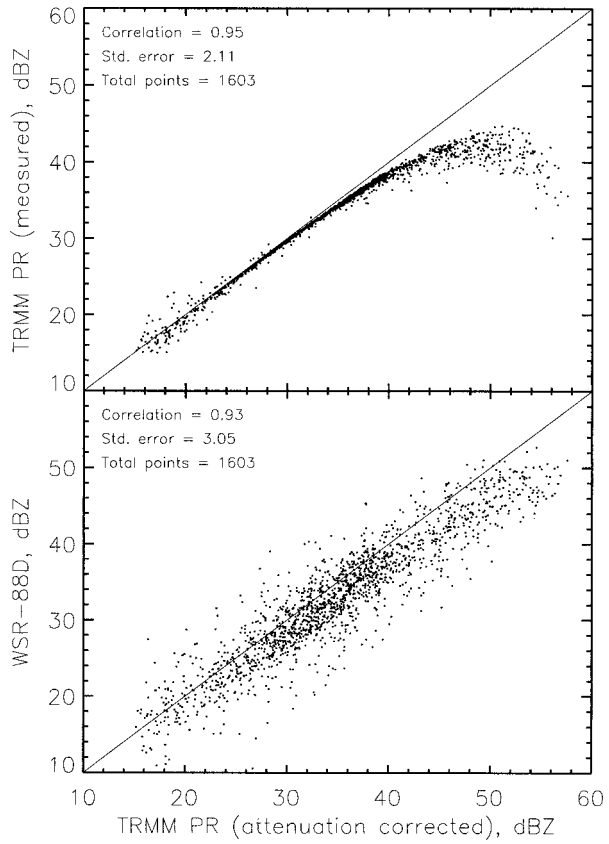

FIG. 3. Scatterplots of radar reflectivity factors at a height of 3 km derived from data in 4 km × 4 km × 1.5 km resolution cells for the case shown in Fig. 1. (top) Plot of dBZ values of the PR without attenuation correction vs the same quantity with attenuation correction. (bottom) Plot of dBZ values from WSR-88D vs dBZ values from the PR with attenuation correction.

values from the GV coordinates onto the common grid.

3. Comparisons of radar reflectivity factors

In the TRMM PR output data products, two kinds of radar reflectivity factors are available: the measured radar reflectivity factor, Z_m (data product 1c-21), and the attenuation-corrected radar reflectivity factor, or simply radar reflectivity factor, Z (data product 2a-25). The two quantities are related approximately by the equation

$$P(r) = C|K|^2 Z_m(r)/r^2 = C|K|^2 Z(r) \exp\left[-0.2 \ln 10 \int_0^r k(s)\, ds\right] \Big/ r^2, \quad (1)$$

where $P(r)$ is the radar return power at range r, k is the specific attenuation (dB km^{-1}), C is the radar constant, and $|K|^2$ is the dielectric factor of water which, by convention, is taken to be 0.93. At ranges near the surface, $Z_m(r)$, may be dominated by the surface return. A surface-clutter routine in algorithm data product 1c-21 is used to eliminate these data before correction for attenuation and estimation of rain rate. It should also be pointed out that a beamfilling correction factor is also used in estimating dBZ from the PR data (Iguchi et al. 2000; Kozu and Iguchi 1999). Since this correction term is usually small, for purposes of the paper we will interpret difference between $\mathrm{dB}Z_m$ and dBZ entirely as an attenuation correction. The PR attenuation correction method itself is a hybrid of the Hitschfeld–Bordan (Hitschfeld and Bordan 1954) and the surface reference techniques (Meneghini et al. 2000). Details of the procedure can be found in Iguchi et al. (2000) and Iguchi and Meneghini (1994).

a. Case study

On 9 March 1998 an intense squall line moving over the Melbourne WSR-88D site coincided with a TRMM overpass. The dBZ values measured by the WSR-88D and PR are shown in Fig. 1 for a height above the surface of 3 km. The three panels show maps of $\mathrm{dB}Z_m$ (top), dBZ (center), and $\mathrm{dB}Z_{\mathrm{GV}}$ (bottom) where the resolution cell for all products is 4 km × 4 km × 1.5 km. (In this paper, quantities derived from the WSR-88D data are denoted by the subscript GV—ground validation.) A similar set of plots is shown in Fig. 2 but at a height of 1.5 km. Note that the common area, the area observed by both radars, is smaller in this case because of earth-curvature and surface-clutter effects in the WSR-88D and surface-clutter effects at off-nadir incidence angles in the PR. Surface contamination in the PR return manifests itself as an enhancement of the radar return along parallel lines near the edges of the swath, an effect that can be seen clearly in the top panel of Fig. 2. For the results presented in the paper, volume elements where the surface clutter dominates are discarded.

Differences between the results shown in the top and center panels of Figs. 1 and 2 can be interpreted primarily as the change in the radar reflectivity factors after attenuation correction is introduced. A more quantitative way of displaying the differences is shown in Figs. 3 and 4, where scatterplots of $\mathrm{dB}Z_m$ versus dBZ (top) and $\mathrm{dB}Z_{\mathrm{GV}}$ versus dBZ (bottom) are shown at heights of 3 and 1.5 km, respectively.

The scatterplot of $\mathrm{dB}Z_m$ versus dBZ at a height of 6 km (not shown) indicates that the two quantities are nearly identical and that the attenuation from the storm top to a 6-km height is usually negligible even in an intense rain case such as this. In descending from 6 to 3 km (Fig. 3) we find a strong increase in the apparent attenuation suffered by the PR signal. Examination of the data in Fig. 3 (top) shows that for dBZ values greater than about 40 dB, the attenuation correction often exceeds 10 dB and can be as large as 26 dB. Scatterplots of the corrected dBZ and the $\mathrm{dB}Z_{\mathrm{GV}}$ data shown in Fig. 3 (bottom) indicate that the two quantities are well correlated, with a correlation coefficient, ρ, of 0.93. On the other hand, attenuation correction gives dBZ values that, on average, are 2.1 dB greater than those obtained from

TABLE 3. Mean radar reflectivity factors of the WSR-88D (dBZ_{GV}) and the PR with (dBZ) and without (dBZ_m) attenuation correction for the 24 overpass cases at a height of 3 km.

Date	Mean			Correlation		Points
	$\langle dBZ_m \rangle$	$\langle dBZ \rangle$	$\langle dBZ_{GV} \rangle$	dBZ_m–dBZ_{GV}	dBZ–dBZ_{GV}	(N_i)
24 Jan 1998	30.36	31.67	31.31	0.86	0.88	470
17 Feb 1998	34.04	35.37	33.6	0.87	0.88	1471
9 Mar 1998	33.05	35.02	32.90	0.89	0.93	1603
18 Mar 1998	27	27.9	27.5	0.88	0.90	390
30 Apr 1998	20.47	20.89	19.95	0.69	0.73	452
4 May 1998	31.27	31.69	30.93	0.92	0.92	974
6 Jul 1998	32.27	36.77	33.8	0.76	0.84	163
8 Jul 1998	26.6	28.37	28.75	0.74	0.76	194
10 Jul 1998	27.9	28.67	28.08	0.82	0.82	430
13 Jul 1998	27.23	28.38	29.69	0.86	0.89	621
15 Jul 1998	24.93	25.77	27.08	0.83	0.87	557
18 Jul 1998	31.06	33.38	30.94	0.71	0.73	94
22 Jul 1998	28.47	29.83	29.83	0.80	0.84	186
2 Aug 1998	27.29	28.68	28.13	0.87	0.89	229
4 Aug 1998	27.53	28.77	27.65	0.85	0.87	253
5 Aug 1998	27.76	28.65	29.31	0.88	0.90	525
9 Aug 1998	28.23	30.3	29.5	0.79	0.82	259
15 Aug 1998	30.92	34.42	32.96	0.77	0.87	212
20 Aug 1998	30.78	32.6	31.92	0.86	0.90	623
22 Aug 1998	25.61	26.58	26.46	0.84	0.87	720
18 Sep 1998	27.61	28.71	28.29	0.83	0.86	807
25 Sep 1998	28.87	30.64	30.99	0.82	0.85	335
18 Oct 1998	21.54	22.02	19.75	0.53	0.57	127
5 Nov 1998	25.57	25.86	24.12	0.89	0.90	2090
Total	28.75	29.92	29.05	0.87	0.90	13 785

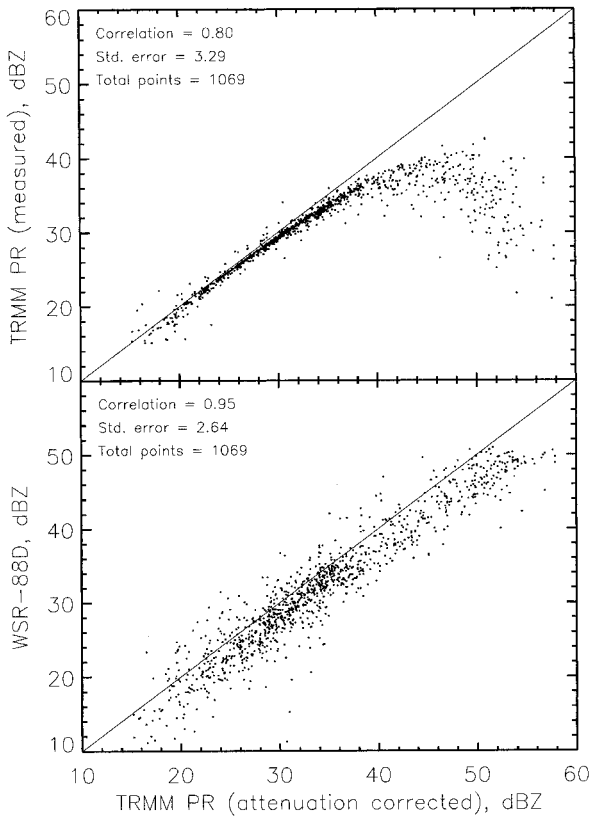

FIG. 4. Same as Fig. 3 except at a height of 1.5 km for the case shown in Fig. 2.

the WSR-88D. Using angular brackets to denote the mean value, the results are the following: $\langle dBZ_m(h = 3\ km) \rangle = 33.05$ dB, $\langle dBZ(h = 3\ km) \rangle = 35.02$ dB, and $\langle dBZ_{GV}(h = 3\ km) \rangle = 32.90$ dB. These trends persist as the height is changed from 3 to 1.5 km (Fig. 4). At this near-surface altitude, the maximum difference between dBZ_m and dBZ is nearly 40 dB (Fig. 4, top). Despite the presence of strong attenuation, the corrected dBZ values are well correlated with the dBZ_{GV} values, $\rho = 0.95$, whereas the correlation coefficient between dBZ_m and dBZ_{GV} is 0.78. As in the 3-km case, however, the mean value of the PR-derived reflectivity factor with attenuation correction is over 2 dB larger than that derived from the GV radar: $\langle dBZ_m(h = 1.5\ km) \rangle = 30.64$ dB, $\langle dBZ(h = 1.5\ km) \rangle = 34.25$ dB, and $\langle dBZ_{GV}(h = 1.5\ km) \rangle = 32.04$ dB. As discussed in the next section, some of the discrepancies between dBZ_{GV} and dBZ can be attributed to non-Rayleigh scattering effects at the higher frequency, different viewing geometries, and attenuation effects in the WSR-88D.

b. Non-Rayleigh scattering and related effects

The primary reasons for comparing data from the PR and ground-based radars are to determine the relative calibration accuracy of the radars and to assess the performance of the attenuation correction and rain-rate estimation procedures used in the PR algorithms. There are a number of factors that interfere with achieving these objectives, however. One source of error arises

TABLE 4. Mean radar reflectivity factors of the WSR-88D (dBZ_{GV}) and the PR with (dBZ) and without (dBZ_m) attenuation correction for the 24 overpass cases at a height of 1.5 km.

Date	Mean			Correlation		Points
	$\langle dBZ_m \rangle$	$\langle dBZ \rangle$	$\langle dBZ_{GV} \rangle$	dBZ_m–dBZ_{GV}	dBZ–dBZ_{GV}	(N_i)
24 Jan 1998	30.81	33.22	33.99	0.76	0.84	234
17 Feb 1998	33.04	35.68	33.65	0.89	0.93	969
9 Mar 1998	30.64	34.25	32.04	0.78	0.95	1069
18 Mar 1998	26.86	28.23	27.68	0.89	0.92	339
30 Apr 1998	22.76	23.49	23.15	0.75	0.80	333
4 May 1998	30.67	31.66	30.39	0.95	0.95	339
6 Jul 1998	28.98	32.84	30.57	0.87	0.90	46
8 Jul 1998	24.78	26.37	26.41	0.57	0.60	57
10 Jul 1998	27.4	28.26	27.79	0.79	0.79	129
13 Jul 1998	26.08	27.47	28.49	0.84	0.88	108
15 Jul 1998	25.38	26.61	27.77	0.82	0.85	197
18 Jul 1998	29.2	32.38	26.58	0.62	0.67	43
22 Jul 1998	27.95	29.55	31.01	0.78	0.84	116
2 Aug 1998	26.67	28.62	27.73	0.80	0.84	106
4 Aug 1998	26.53	28.09	27.04	0.84	0.87	197
5 Aug 1998	28.53	29.6	28.37	0.87	0.88	249
9 Aug 1998	27.69	30.39	29.04	0.76	0.81	115
15 Aug 1998	29.94	35.23	33.94	0.72	0.87	129
20 Aug 1998	30.07	31.91	30.74	0.85	0.89	192
22 Aug 1998	23.74	24.9	24.31	0.77	0.82	278
18 Sep 1998	27.11	28.78	27.81	0.79	0.87	387
25 Sep 1998	27.64	30.86	31.03	0.82	0.88	128
18 Oct 1998	25.02	25.82	25.29	0.66	0.68	168
5 Nov 1998	26.74	27.12	25.9	0.93	0.93	1121
Total	28.43	30.30	29.18	0.84	0.90	7049

from inaccuracies in geolocation. The location of a particular PR radar volume along the beam is computed from the latitude and longitude of the estimated surface range gate, normally taken as that gate where the return power is maximum. [The actual determination of the surface is somewhat more involved; details can be found in Kozu et al. (2001)]. Errors in these data and variations in topography contribute to uncertainties in the location of the PR radar volume relative to that of the GV volume.

Apart from the problem of matching the radar volumes in space and time is the issue of non-Rayleigh scattering effects at the PR frequency. Increases in the radar reflectivity factor are usually associated with an increase in the number concentration of large particles, the backscattering cross sections of which can be significantly different for the 10-cm wavelength of the WSR-88D and the 2.17-cm wavelength of the PR. This non-Rayleigh scattering effect can be estimated using measured DSDs. For this purpose we employ DSDs measured in Switzerland (courtesy of Dr. Matthias Steiner). The results can be summarized by the mean difference, Δ_X, between the radar reflectivity factors at 13.8 GHz (PR) and 3 GHz (WSR-88D), given that the radar reflectivity factor at 3 GHz exceeds a threshold of X dBZ:

$$\Delta\hat{X} = \langle \mathrm{dBZ}(13.8\ \mathrm{GHz}) | \mathrm{dBZ}(3\ \mathrm{GHz}) > X \rangle - \langle \mathrm{dBZ}(3\ \mathrm{GHz}) | \mathrm{dBZ}(3\ \mathrm{GHz}) > X \rangle. \quad (2)$$

For spherical particles, the results are shown in the first section of Table 1. For example, for the 3309 DSDs for which dBZ(3 GHz) $>$ 30 dBZ, the mean difference between the 13.8- and 3-GHz radar reflectivity factors is 0.767 dB, where the mean dBZ(3 GHz) is 34.47 dBZ. A secondary effect arises from the fact that raindrops are nonspherical. Letting $2b$ and $2a$ represent the lengths of the major and minor axes of the oblate then, using the relationship of Pruppacher and Beard (1970), the ratio of a and b is given by

$$a/b = 1.03 - 0.062\, D_{\mathrm{eq}}, \quad (3)$$

where D_{eq} is the diameter (mm) of the equivolume sphere. To perform the calculations we assume that the GV radar beam is directed along the horizon with either horizontal or vertical polarization, while the PR incidence is nadir-directed. Particle canting is neglected so that the symmetry axis of the particles is assumed to be along the vertical. The results of the table show that if the ground-based radar is horizontally polarized then Δ_X is approximately the same for oblates as for spheres. Since the WSR-88D is horizontally polarized, these results are relevant to the comparisons presented here. For vertical polarization, Δ_X increases substantially relative to the other cases where we find that for dBZ(3 GHz) $>$ 35 dBZ, the average dBZ at 13.8 GHz exceeds that at 3 GHz by nearly 3 dB.

A third cause of discrepancies between the PR and GV arises from signal attenuation in the GV radar. Although this effect usually can be neglected at S band, in the 9 March 1998 case discussed in the previous

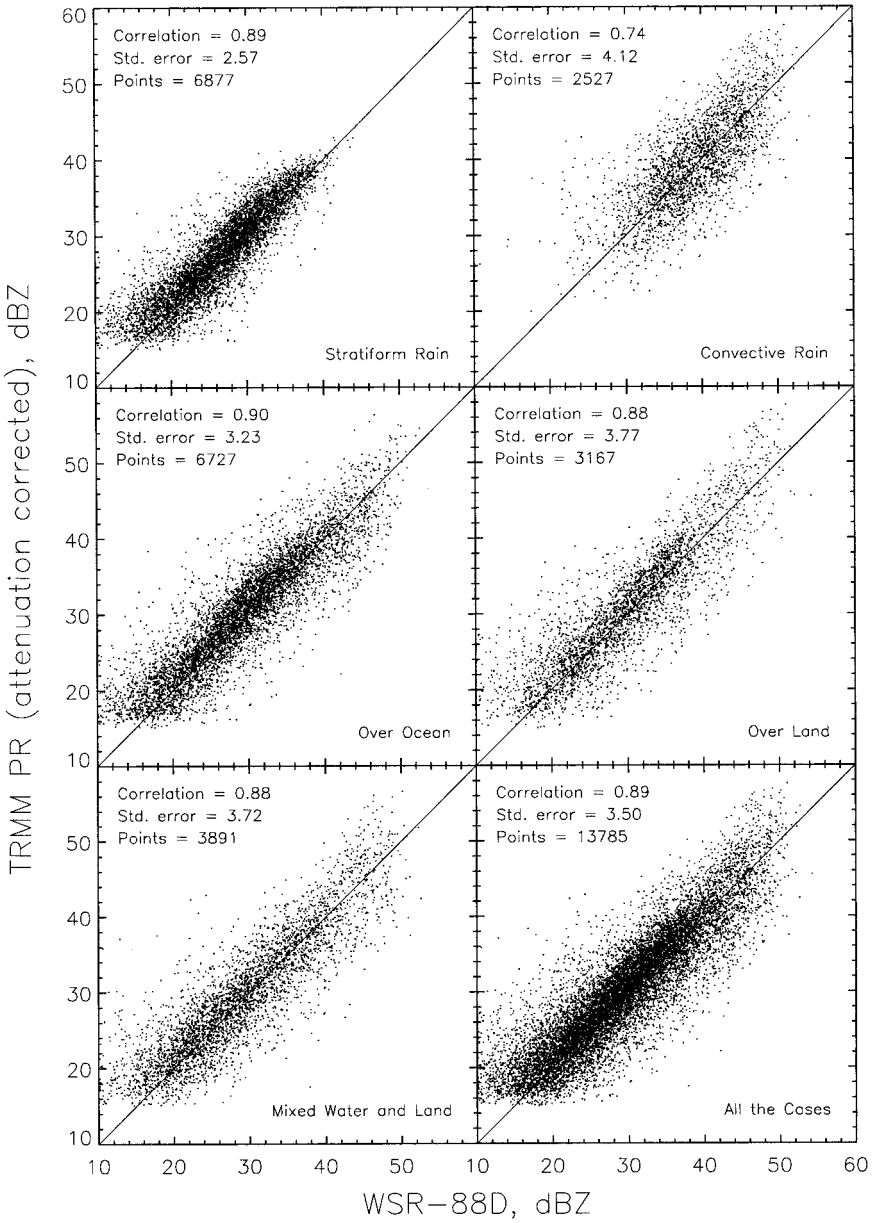

FIG. 5. Scatterplots of dBZ from PR (with attenuation correction) with those from the WSR-88D from all overpasses conditioned on rain type or surface background type. The unconditioned results are shown in the lower right-hand plot.

section, and for several other overpasses during the year, strong rain was present along a radial sector (see Figs. 1 and 2). From the drop size distributions described above, we find specific attenuation–rain rate (k–R) relationships at 3 GHz of $k = 3.88 \times 10^{-4} R^{0.91}$ at $T = 20$°C and $k = 6.68 \times 10^{-4} R^{0.91}$ at $T = 0$°C. Battan (1973) quotes one-way path attenuations per unit mm h^{-1} [(dB km^{-1})/(mm h^{-1})] at 3 GHz that range from a low of 3×10^{-4} to a high of 9.2×10^{-4}. For example, for a rain rate of 20 mm h^{-1} over a 50-km path, the signal can be expected to produce a two-way path attenuation between 0.6 and 1.84 dB. This simple example shows that attenuation is not always negligible at S band (Ryzhkov and Zrnic 1995) and, like the non-Rayleigh scattering effect, serves to increase the discrepancy (assuming perfect measurements) between the radar reflectivities derived from the PR and WSR-88D.

We conclude from the above considerations that the most important correction factor is the effect of non-Rayleigh scattering at the PR frequency. The correction is nonlinear so that it must be applied at the level of the common-resolution data and not to the mean dBZ. Processing of other drop size distributions shows that the results depend, not surprisingly, on the particular

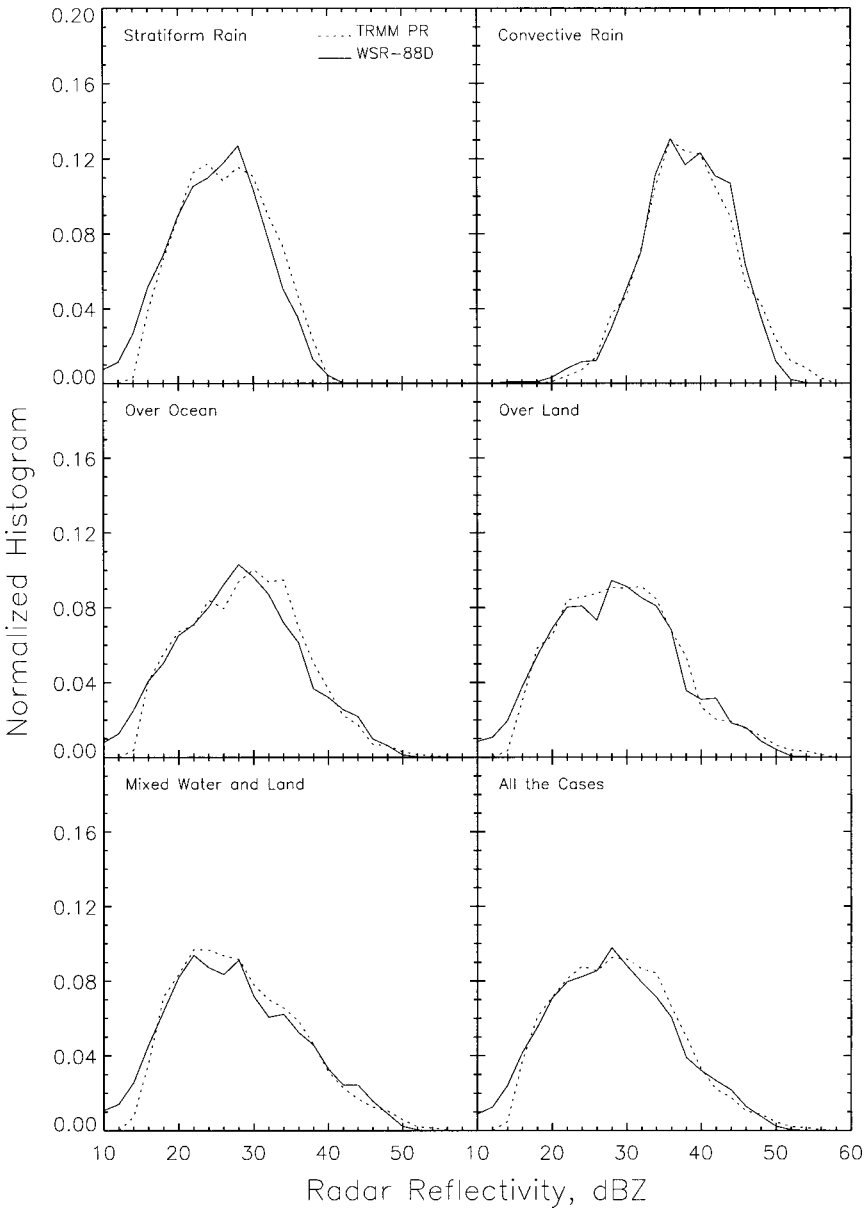

FIG. 6. Histograms of dBZ for the attenuation-corrected PR (dashed lines) and WSR-88D (solid lines) for the same categories used in Fig. 5.

set of DSDs used. Because of this, and the fact that the correction is relatively small for the majority of data, a modification of the PR data to account for non-Rayleigh scattering is not made in this paper. It should be noted, finally, that because the PR algorithm accounts for non-Rayleigh scattering effects in the selection of the *R–Z* relationship, correction at the dBZ level is not required in the estimation of rain rate (Iguchi et al. 2000).

4. Statistical comparisons

a. dBZ comparisons

The set of all data collected at a height of 3 km from the 24 overpasses of the Melbourne site during 1998 is shown in the scatterplots of Fig. 5. Data points included in the plots are those for which $\mathrm{dBZ}_m > 15$ dBZ and $\mathrm{dBZ}_{\mathrm{GV}} > 10$ dBZ. Consequently, if either the WSR-88D or PR does not detect rain at a particular element, the data are discarded. For the area-averaged rain rates considered later in the paper, this restriction is not enforced and the two datasets are processed independently. It should be noted that although the nominal threshold of the PR is 18 dBZ, the radar return power is obtained by subtracting the signal-plus-noise from a noise-only estimate. Because both quantities are random variables, values of dBZ_m below the threshold are sometimes encountered. The effect on the statistics from a change in

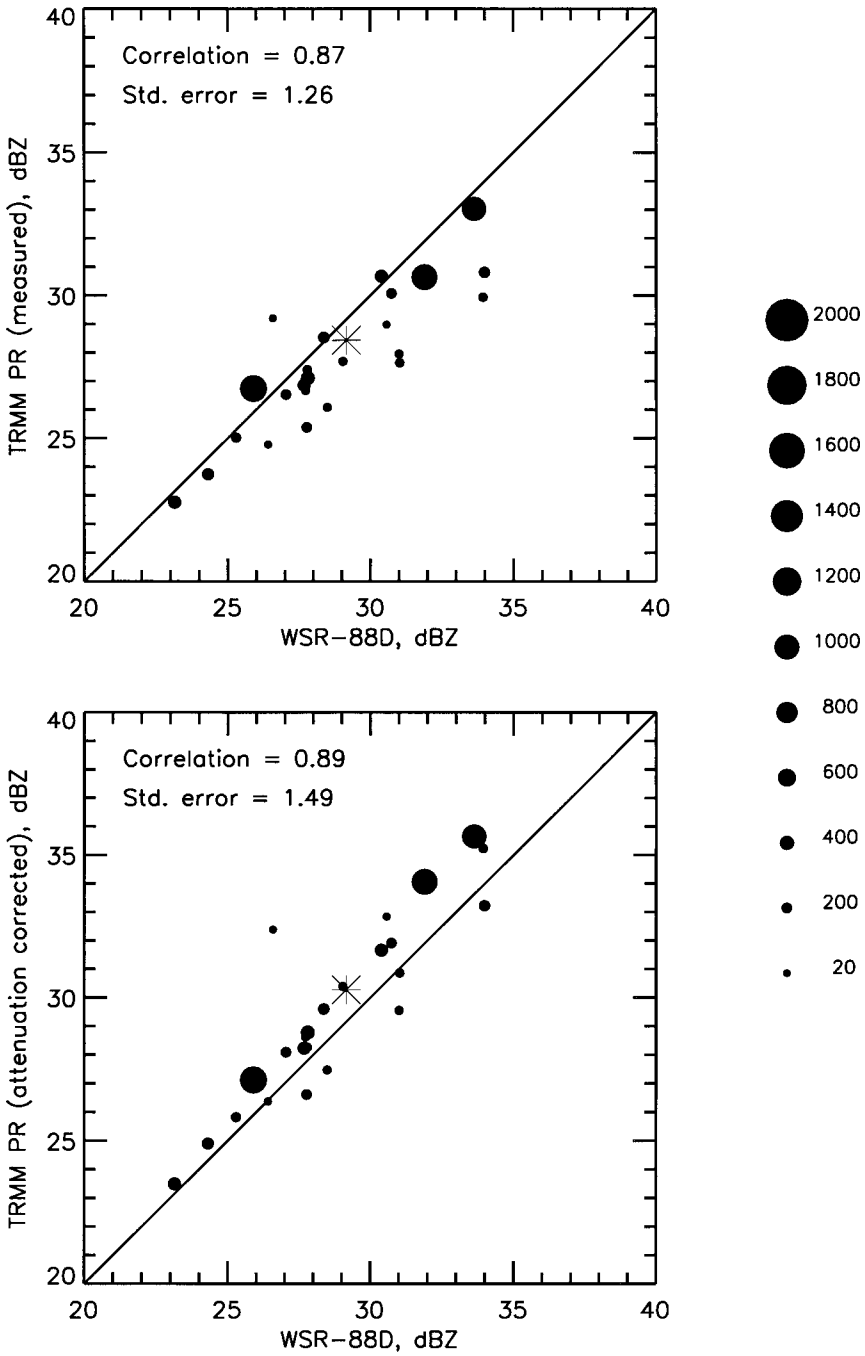

FIG. 7. Mean of the PR-derived radar reflectivities (top) without and (bottom) with attenuation correction vs the mean of the WSR-88D radar reflectivities at a height of 1.5 km. Each data point represents an overpass event. The size of the data point is proportional to the number of common-resolution cells in the overlap region for which $dBZ_{PR} > 15$ dBZ and $dBZ_{GV} > 10$ dBZ. Asterisks represent the weighted means of the datasets.

the threshold values will be discussed at the end of this section.

The correlation coefficient of dBZ and dBZ_{GV} for the entire set of 13 785 elements from the 24 overpasses is 0.90 (lower right-hand panel of Fig. 5). Scatterplots are also shown for divisions of the data into rain type (stratiform and convective—top panels) and surface background type (ocean, land, and coastal—middle and bottom-left panels). While the surface background classification can be applied to both datasets, this is not the case for the rain-type classification where different methods are used to analyze the PR and GV data (Awaka

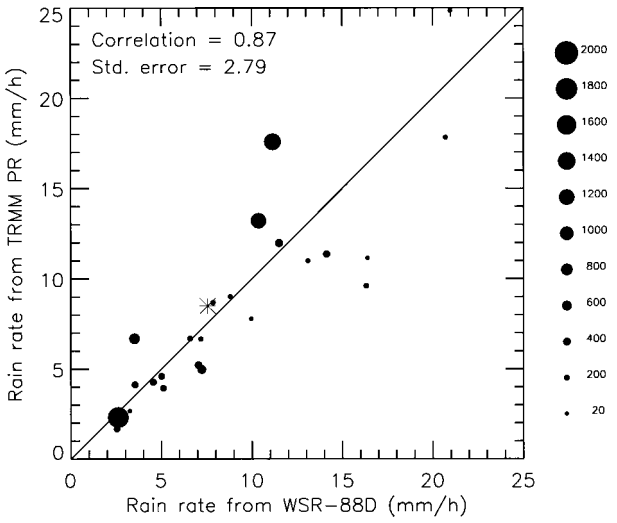

FIG. 8. Mean of the PR-derived rain rate vs the mean of the WSR-88D–derived rain rate. Each data point represents an overpass event. The size of the data point is proportional to the number of high-resolution cells in the overlap region for which both the PR- and GV-derived rain rates are greater than zero. The asterisk represents the weighted means of the datasets.

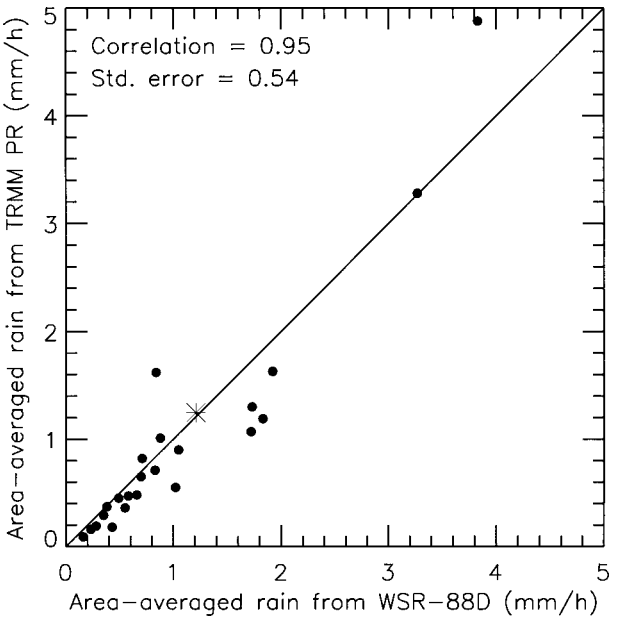

FIG. 9. Estimates of area-averaged rain rate from the PR and WSR-88D data for the 24 overpasses. The asterisk gives the mean of the data.

et al. 1998; Steiner et al. 1995). Because of this, the data plotted in the top panels of Fig. 5 comprise only those pixels for which the GV and PR classifications are in agreement; for example, the points plotted for stratiform rain correspond to elements for which both the GV and PR algorithms classify the rain as stratiform. These issues are discussed in more detail in the next section. A glance at the scatterplots for stratiform and convective rain shows that the data are more highly correlated for stratiform ($\rho = 0.89$) than for convective ($\rho = 0.74$) rain and that the mean dBZ in stratiform rain ($\langle \mathrm{dBZ} \rangle = 28.37$ dBZ, $\langle \mathrm{dBZ_{GV}} \rangle = 27.11$ dB) is significantly lower than that for convective rain ($\langle \mathrm{dBZ} \rangle = 39.65$ dBZ, $\langle \mathrm{dBZ_{GV}} \rangle = 39.11$ dBZ). In contrast, the division of data into ocean and land do not reveal any obvious differences, with correlations and means approximately the same. Histograms of the dBZ and $\mathrm{dBZ_{GV}}$ data for the six categories are pictured in Fig. 6, showing that the distributions of dBZ for the PR and GV data are in good agreement for all categories. Unlike the scatterplots where the data are compared element by element, the histograms are insensitive to registration errors.

The data in Figs. 5 and 6 are limited to a height of 3 km. The results, moreover, do not include the PR radar reflectivity factors before attenuation correction, dBZ_m. Tables 2–4, which summarize the comparisons at heights of 6, 3, and 1.5 km, give a more complete picture of the PR results relative to the GV both before and after attenuation correction. Listed in each table are the means and correlation coefficients for dBZ_m, dBZ, and $\mathrm{dBZ_{GV}}$ for the 24 overpasses as well as the weighted mean values, given on the last line of each table. The weighted mean is defined by

$$\langle \mathrm{dBZ} \rangle_W = \sum_{i=1}^{24} N_i \langle \mathrm{dBZ} \rangle_i \Big/ \sum_{i=1}^{24} N_i, \qquad (4)$$

where N_i, is the number of common resolution elements in the ith overpass for which $\mathrm{dBZ_{GV}} > 10$ dB and dBZ > 15 dB. The quantity $\langle \mathrm{dBZ} \rangle_i$ is the mean value taken over the N_i elements.

It is instructive to look at the differences in the weighted means as a function of height using the following notation: $\Delta(A, B) \equiv \langle A \rangle_W - \langle B \rangle_W$. For example, $\Delta(\mathrm{dBZ}_m, \mathrm{dBZ_{GV}}) = \langle \mathrm{dBZ}_m \rangle_W - \langle \mathrm{dBZ_{GV}} \rangle_W$. We find that $\Delta(\mathrm{dBZ}, \mathrm{dBZ_{GV}}) = 0.79$, 0.87, and 1.12 dB at heights of 6, 3, and 1.5 km, respectively. The results suggest that the difference between the attenuation-corrected PR and the WSR-88D data is relatively insensitive to height and that the PR data are generally about 1 dB greater than the GV. To get an indication of the effect of attenuation correction on the PR results, consider $\Delta(\mathrm{dBZ}, \mathrm{dBZ}_m)$, the difference between the dBZ values from the PR with and without attenuation correction. We find that $\Delta(\mathrm{dBZ}, \mathrm{dBZ}_m) = 0.24$ dB (6 km), 1.17 dB (3 km), and 1.87 dB (1.5 km); that is, the average attenuation correction goes from 0.24 dB at 6 km to 1.87 dB at 1.5 km. If a power-law relationship $Z = aR^b$ is used to compute rain rate, then the ratio of rain rates that would be derived with (R_w) and without attenuation correction (R_{wo}) can be written

$$R_{\mathrm{w}}/R_{\mathrm{wo}} = \exp[0.1 \ln 10 \; b^{-1} \Delta(\mathrm{dBZ}, \mathrm{dBZ}_m)], \qquad (5)$$

which, for small values of the exponent, is approxi-

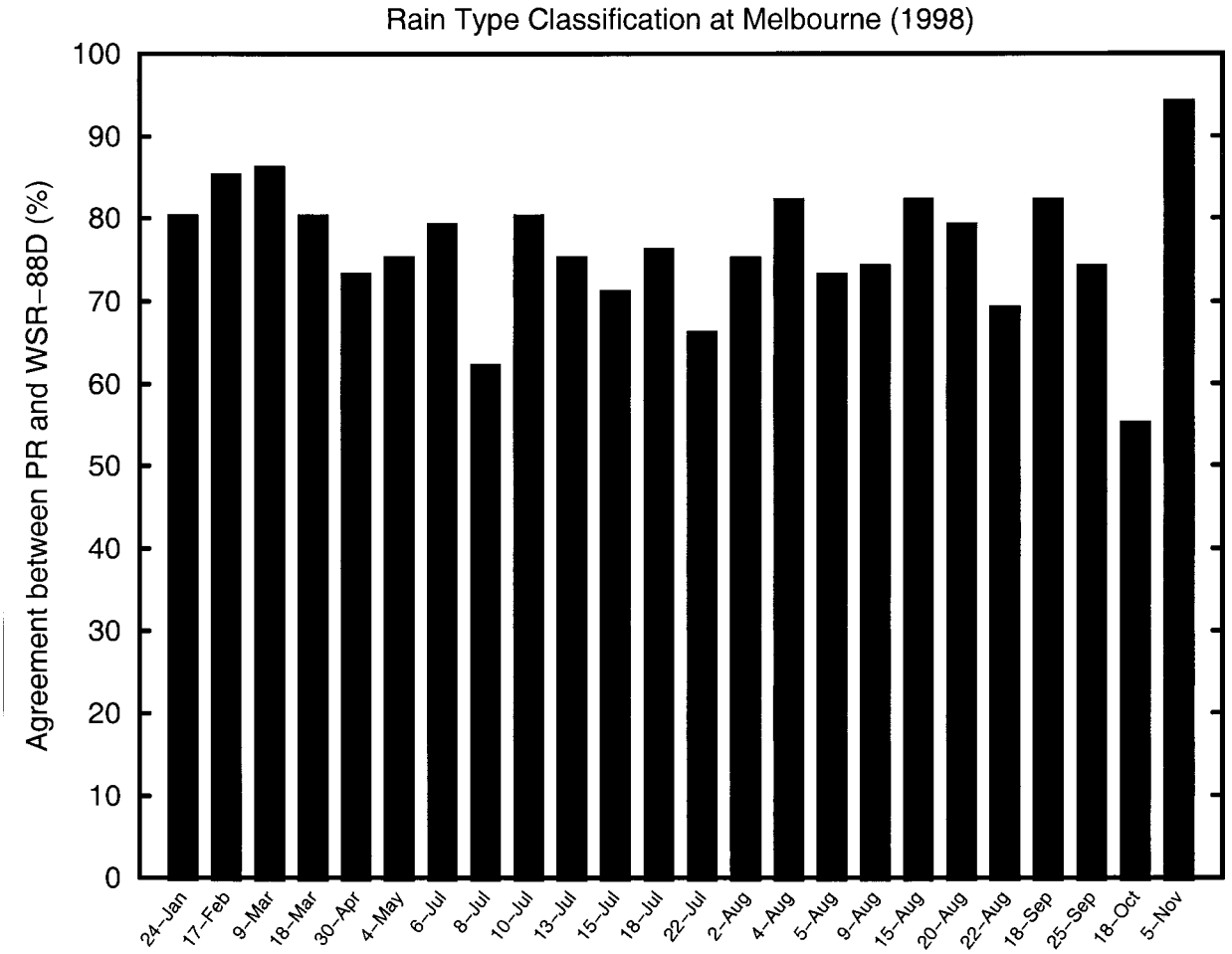

FIG. 10. Agreement between the PR and WSR-88D rain-type classification for the 24 overpasses. "Agreement" is defined as the ratio of the rain area where the PR and GV classifications agree to the total rain area.

mately $1 + 0.1 \ln(10)\, \Delta(\mathrm{dBZ}, \mathrm{dBZ}_m)/b$. For example, if $b = 1.5$, we find that the mean rain rate, using the attenuation-corrected dBZ, is about 19% larger at 3 km and 32% larger at 1.5 km than what would be found if attenuation correction was not used. It should be noted that because of the nonlinearity between Z and R, these results are approximate. Globally, the effect of the PR attenuation correction has been estimated to increase the rain rate estimates by about 25% at a height of 2 km above the surface (Meneghini et al. 2001).

The statistics in Tables 2–4 were found by thresholding the PR data at 15 dBZ and the GV data at 10 dBZ. Although all PR rain data exceed 15 dBZ, GV rain data below the 10 dBZ threshold do exist and it is natural to ask how a change in the GV threshold would affect the statistics. As we note above, with a 10 dBZ threshold on the GV data, $\Delta(\mathrm{dBZ}, \mathrm{dBZ}_{\mathrm{GV}}) = 1.12$ dB, $N = 7049$ at 1.5 km and $\Delta(\mathrm{dBZ}, \mathrm{dBZ}_{\mathrm{GV}}) = 0.83$ dB, $N = 13\,785$ at 3 km, where N is the number of data points. If we increase the GV threshold to 15 dBZ we obtain $\Delta(\mathrm{dBZ}, \mathrm{dBZ}_{\mathrm{GV}}) = 0.92$, $N = 6824$ at 1.5 km and $\Delta(\mathrm{dBZ}, \mathrm{dBZ}_{\mathrm{GV}}) = 0.68$ dB, $N = 13\,347$ at 3 km. These results indicate that an increase in the GV threshold level to 15 dBZ, the same as the PR threshold, decreases the average difference at the 1.5 and 3-km levels. On the other hand, if we use all GV rain data, irrespective of the dBZ value, we find $\Delta(\mathrm{dBZ}, \mathrm{dBZ}_{\mathrm{GV}}) = 1.35$ dB, $N = 7173$ at 1.5 km, and $\Delta(\mathrm{dBZ}, \mathrm{dBZ}_{\mathrm{GV}}) = 1.06$ dB, $N = 13\,971$ at 3 km. Clearly, if we do not threshold the GV data, the mean difference between the PR and GV increases because pairs of points will be included in the statistics for which $\mathrm{dBZ} > 15$ dBZ and $\mathrm{dBZ}_{\mathrm{GV}} < 10$ dBZ so that the difference is at least 5 dB.

A summary of the results at a 1.5-km height, using the standard dBZ thresholds, is depicted in Fig. 7. In the top panel a scatterplot of the mean of dBZ_m versus the mean of $\mathrm{dBZ}_{\mathrm{GV}}$ is shown for the 24 overpasses. The size of each data point has been made proportional to the number of common-resolution elements (4 km × 4 km × 1.5 km) in the overpass for which $\mathrm{dBZ}_m > 15$ dBZ and $\mathrm{dBZ}_{\mathrm{GV}} > 10$ dBZ. A similar plot is shown in the bottom panel but where dBZ has replaced dBZ_m as the dependent variable. The asterisk in each plot represents the weighted means of the relevant datasets. The

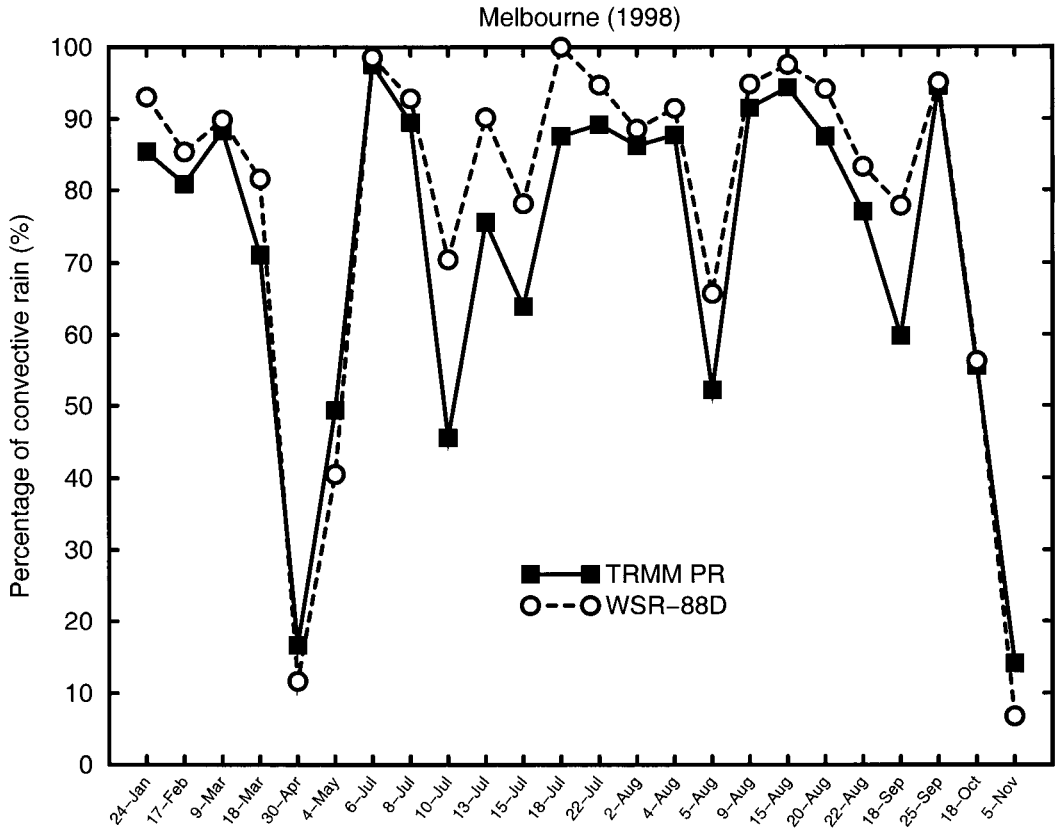

FIG. 11. Percentage of the total rain volume contributed by convective rain for the PR (solid) and WSR-88D (dashed). Note that the total rain volume is computed independently from the WSR-88D and PR data.

correlation coefficient and standard error displayed on each plot are computed by assuming that each data point (overpass) is weighted equally. It should be noted that this quantity is not the same as the correlation coefficient given in the tables, where each common-resolution element is weighted equally. In the former case, from Fig. 7, $\rho(\mathrm{dB}Z, \mathrm{dB}Z_{\mathrm{GV}}) = 0.89$ and $\rho(\mathrm{dB}Z_m, \mathrm{dB}Z_{\mathrm{GV}}) = 0.87$, while in the later case, from Table 4, $\rho(\mathrm{dB}Z, \mathrm{dB}Z_{\mathrm{GV}}) = 0.90$ and $\rho(\mathrm{dB}Z_m, \mathrm{dB}Z_{\mathrm{GV}}) = 0.84$.

b. PR–GV rain rate comparisons

If the same *Z–R* relationship was used to estimate rain rates from the ground-based and spaceborne data, the results could be obtained in a straightforward manner from the *Z* results. This is not the case, however. The comparison is further complicated by the fact that the PR and WSR-88D rain-rate algorithms employ different stratiform–convective classifications and different *Z–R* relationships for each class. In this section we begin with comparisons of the rain rates irrespective of rain classification. This is followed by results on the classification agreement between the two radars and comparisons of fractional rainfall amounts from convective and stratiform rain.

Shown in Fig. 8 are the mean rain rates derived from the PR and GV common-resolution data for the 24 overpasses. For each overpass, the mean is computed from those elements at which both the PR and WSR-88D detect rain. As in Fig. 7, each point in the scatterplot represents the mean value from a particular overpass where the size of the data point is proportional to the number of raining elements in the common area. In performing the comparisons at each pixel, the near-surface rain rate from the PR data product is compared with the GV rain-rate product at a height of approximately 1.5 km. Because of surface-clutter effects, the near-surface rain rate derived from the PR is a function of incidence angle so that the spatial matching of the PR and GV datasets are probably less accurate than in the dB*Z* comparisons. Although the weighted means of the derived rain rates are in reasonably good agreement ($\langle R_{\mathrm{PR}}\rangle_W = 8.5$ mm h^{-1}, $\langle R_{\mathrm{GV}}\rangle_W = 7.6$ mm h^{-1}), the scatter is relatively high. These variations arise from several sources: registration errors, differences in the radar reflectivities, and differences in the *Z–R* relationships that are applied to these dB*Z* fields.

A somewhat different way to present the comparisons is to compute the instantaneous area-average rain rate from PR and GV (Schumacher and Houze 2000). As in the previous case, only the area defined by the intersection of the PR and GV scans is considered. In con-

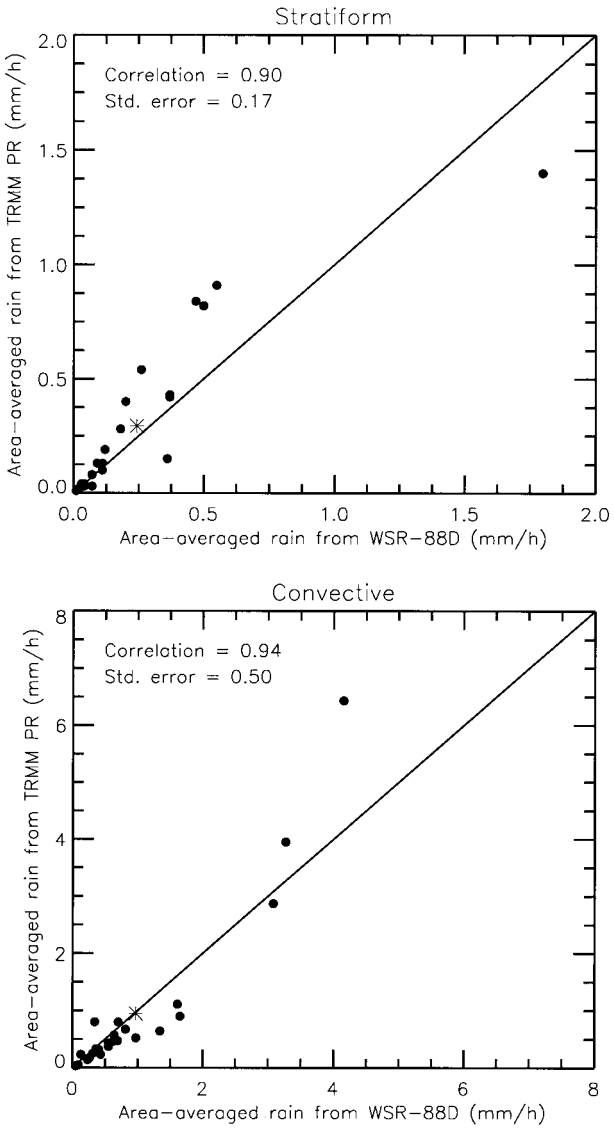

FIG. 12. Same as Fig. 9 except that the area averages are computed separately over stratiform and convective regions. The stratiform (convective) area is defined as the set of the common-resolution elements over which both the GV and PR classify the rain type as stratiform (convective).

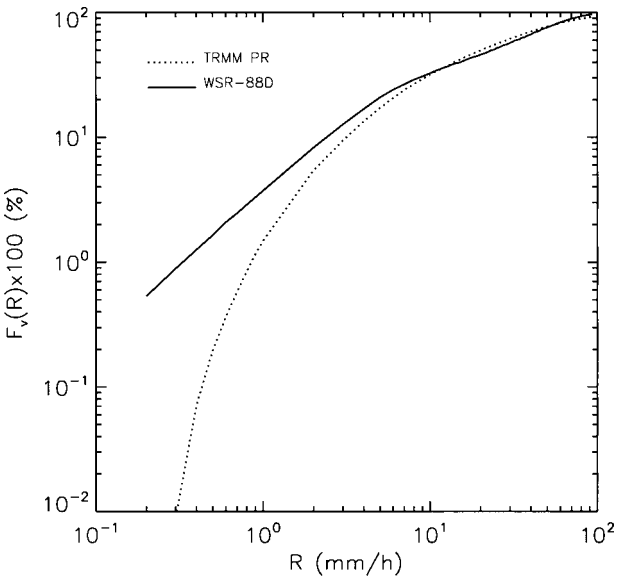

FIG. 13. Fractional rainfall by volume, $F_v(R)$, vs rain rate R for the WSR-88D and PR datasets.

trast, however, the PR and GV calculations are done independently so that the requirement that rain be detected by both radars at a given 4 km × 4 km element is discarded. The instantaneous area-average rain rate for a particular overpass is computed from

$$R_{\mathrm{AAV}} = M^{-1} \sum_{j=1}^{M} R_j, \tag{6}$$

where the summation is taken over all the (equal area) elements, M, that compose the common viewing area. In contrast to the previous results where the PR and GV data were resampled to a common grid, this is not required (and in fact not done) for the area-average computations. The results are shown in Fig. 9. It is noteworthy that the means of the area-averaged rain rates, represented by the asterisk, are quite close (1.25 mm h^{-1} for the PR and 1.21 mm h^{-1} for the GV) and that the correlation coefficient (0.95) is significantly higher than in the previous case. The improved agreement in the area averages comes about, in part, because the overpasses are weighted equally in computing the means for the entire dataset. Thus, the 9 March case in Fig. 8 (located at $x = 11.2$ mm h^{-1}, $y = 17.7$ mm h^{-1}), which has a large influence on the weighted mean, has a smaller weight in the mean of the area averages. One other reason for the improvement is that the registration errors that arise in matching the PR and GV data over the high-resolution grid are not a factor in the area-average rain-rate comparisons. Variability is also reduced because of spatial averaging.

Although the results shown in Figs. 8 and 9 are encouraging, rain rate is not the only parameter of interest. Stratiform–convective classification has attracted much interest in analysis of TRMM data because of different average latent heating profiles associated with each rain type (Houze 1989; Yuter and Houze 1997; Atlas et al. 2000). Moreover, segmenting the Z–R relationship into rain categories has been promoted as a means to improve rain-rate retrievals (Tokay and Short 1996; Amitai 2000). Comparisons of rain classification from the PR and GV radars are instructive because the classification algorithms are based on different structural characteristics of the reflectivity field. Because the PR has good vertical resolution, particularly at nadir, yet somewhat crude horizontal resolution (4 km × 4 km), the PR classification algorithm relies heavily on brightband detection to indicate the presence of stratiform rain (Awaka et al. 1998). In the absence of a well-defined bright

band, the PR algorithm then relies on a ''standard'' algorithm (Steiner et al. 1995) devised for applications to typical ground-based volume scans where the vertical resolution tends to be coarse and more reliable information is available on the horizontal storm structure.

Shown in Fig. 10 is the classification agreement (in percent) in rain type for the PR and GV radars for the 24 overpasses. As before, only those common-resolution cells are used where both radars detect rain. Apart from one case of very good correspondence (94%) and one of poor correspondence (55%), the classification accuracy for most overpasses is close to the average of 76%. It should be noted that the PR has three classifications: stratiform, convective, and other, whereas only the first two categories are defined in the GV algorithm. Clearly, when the rain type is classified as ''other'' by the PR it cannot agree with the GV designation. However, for the data obtained from the overpasses, the percentage rain in this category is a small fraction of the total.

Figure 11 shows the estimated percentage of total rainfall contributed by convective rain as determined independently by the PR and GV. Although the correlation is good, 0.95, the PR classifies a somewhat smaller percentage of the rain as convective (73%) than does the GV (78%). The corresponding instantaneous area-average rain rates for stratiform (top) and convective (bottom) are shown in Fig. 12. When compared to the results in Fig. 9, where the area-averaged rain rates are computed irrespective of rain type, the conditional results show a slight decrease in the correlation. The stratiform category in particular shows a smaller correlation coefficient ($\rho = 0.90$) and larger discrepancy in means ($\langle R\rangle = 0.29$ mm h^{-1}, $\langle R_{\rm GV}\rangle = 0.24$ mm h^{-1}) than does the convective category where $\rho = 0.94$ with $\langle R\rangle = 0.95$ mm h^{-1} and $\langle R_{\rm GV}\rangle = 0.97$ mm h^{-1}.

c. Fractional rain volume

While the statistics discussed above are instructive, they cannot be used to answer the following question: What fraction of the total rainfall does the PR miss because of its low sensitivity at light rain rates? To answer it, let $f_{\rm GV}(R_{\rm GV} \mid R_{\rm GV} > 0)$ denote the probability density function (pdf) of rain rate from the GV, conditioned on rain. The same quantity derived from the PR data is written as $f_{\rm PR}(R_{\rm PR} \mid R_{\rm PR} > 0)$. These conditional pdfs are obtained from the corresponding histograms of the data from the 24 overpasses. It also should be noted that, as in the analysis leading to Fig. 9, the PR and GV datasets are processed independently.

The fractional rain volume contributed by rain rates smaller than R, $F_v(R)$ can be written

$$F_v(R) = \frac{\int_0^R Rf(R \mid R > 0)\, dR}{\int_0^\infty Rf(R \mid R > 0)\, dR}. \qquad (7)$$

Plots of $F_v(R)$ (multiplied by 100) for the GV and PR data are shown in Fig. 13. We can estimate the fraction of the rain volume missed by the PR by comparing F_v at the light rain rates with the corresponding values from the GV. For example, at $R = 0.5$ mm h^{-1}, we have $F_{v-\rm GV}(R = 0.5) - F_{v-\rm PR}(R = 0.5) = 1.4\%$ and $F_{v-\rm GV}(R = 1) - F_{v-\rm PR}(R = 1) = 2.3\%$. These estimates are similar to those obtained by Schmacher and Houze (2000) using the Kwajalein radar–PR datasets (2.3%) and by Bolen and Chandrasekhar (2000) using the S-pol–PR comparisons (3%).

5. Discussion and summary

Critical to assessing the capabilities of the precipitation radar (PR) aboard the TRMM satellite is the determination of the accuracy of the instrument calibration, attenuation correction, and rain-rate estimation. The calibration issue is somewhat easier to address because information can be drawn from the 3-yr records of the internal calibration characteristics and external calibration data using the active radar calibrator. Comparisons of the normalized surface cross section as determined by spaceborne altimeters such as TOPEX and aircraft measurements also have been used to assess the PR calibration. Despite the importance of these measurements, it is ultimately the accuracy of the radar reflectivity factor and the rain-rate estimates that must be established. The focus of the paper is on comparisons of the PR-derived dBZ and rain rates with the same quantities derived from near-simultaneous measurements by the Melbourne WSR-88D.

It can be argued that comparisons of dBZ from the ground-based and spaceborne radars can be used to test the relative calibration of the radars if the data are taken at heights where attenuation effects are negligible (Anagnoustou et al. 2001). If agreement in the means can be established, then comparisons of the dBZ fields at lower heights can be used to check the accuracy of the attenuation correction algorithm. Data from the 24 overpass cases suggest that after attenuation correction the dBZ values are, on average, about 1 dB larger than the WSR-88D values, dB$Z_{\rm GV}$, and that this difference is approximately independent of height. On the other hand, the difference between dB$Z_{\rm GV}$ and dBZ_m (the radar reflectivity factors obtained from the PR without attenuation compensation) and between dBZ and dBZ_m shows a marked height dependence. Use of attenuation correction was estimated to increase the PR-derived rain rates by about 30% at heights of 1.5 km above the surface and by about 20% at a height of 3 km relative to the rain rates that would be derived if an attenuation correction method were not applied.

Two types of rain-rate comparisons were presented. One statistic was derived from comparisons of rain rates over the common-resolution elements of 4 km $\times$ 4 km $\times$ 1.5 km. In essence, this statistic is equivalent to the difference in the conditional mean rain rates at locations

where both radars detect rain. We find that the PR-conditional mean rain rate (8.5 mm h^{-1}) is about 12% larger than the GV-conditional mean (7.6 mm h^{-1}). The picture changes somewhat if we consider the mean of the instantaneous area-average rain rates, where each overpass is weighted equally. In this case, the means are in excellent agreement: 1.25 mm h^{-1} for the PR and 1.21 mm h^{-1} for the GV. Although the equal weighting of each overpass ignores the fact that some overpasses have a much greater rain area, the comparison avoids the registration problem to which the pixel-by-pixel comparisons are subject. It might be noted that a similar type of area-average comparison of the PR data over the Kwajalein radar has also yielded high correlation and excellent agreement in the means (Schumacher and Houze 2000). When the Melbourne WSR-88D and PR data are categorized according to their respective stratiform–convective classifications, good agreement is maintained in convective cases, but the agreement degrades somewhat for stratiform rain where the correlation decreases and the difference in the means increases.

A comprehensive check on the dB*Z* and rain rates derived from the TRMM precipitation radar will require comparisons of multiyear datasets over a variety of well-calibrated ground-truth sites located in different climatological regions. When viewed in this context, the present dataset represents a single data point, and only tentative conclusions can be drawn regarding the accuracy of the attenuation correction and rain-rate estimation algorithms. As more data are gathered and other studies completed, it is expected that a more complete picture of the performance of the precipitation radar will emerge.

Acknowledgments. Our thanks to Dr. Matthias Steiner for the DSD data and to Mike Robinson and Mark Cooley for their assistance with the WSR-88D data. The work was funded under the TRMM Program of NASA HQ.

REFERENCES

Amitai, E., 2000: Systematic variation of observed radar reflectivity–rainfall rate relations in the Tropics. *J. Appl. Meteor.,* **39,** 2198–2208.

Anagnostou, M. S., C. A. Morales, and T. Dinku, 2001: The use of TRMM precipitation radar observations in determining ground radar calibration biases. *J. Atmos. Oceanic Technol.,* **18,** 616–628.

Atlas, D., C. W. Ulbrich, F. D. Marks, R. A. Black, E. Amitai, P. T. Willis, and C. E. Samsury, 2000: Partitioning tropical oceanic convective and stratiform rains by draft strength. *J. Geophys. Res.,* **105,** 2259–2267.

Awaka, J., T. Iguchi, and K. Okamoto, 1998: Early results on rain type classification by the Tropical Rainfall Measuring Mission (TRMM) precipitation radar. *Proc. Eighth URSI Commission F Open Symp.,* Aveiro, Portugal, URSI, 143–146.

Battan, L. J., 1973: *Radar Observation of the Atmosphere.* The University of Chicago Press, 324 pp.

Bolen, S. M., and V. Chandrasekhar, 2000: Quantitative cross validation of space-based and ground-based radar observations. *J. Appl. Meteor.,* **39,** 2071–2079.

Hitschfeld, W., and J. Bordan, 1954: Errors inherent in the radar measurement of rainfall at attenuating wavelengths. *J. Meteor.,* **11,** 58–67.

Houze, R. A., Jr., 1989: Observed structure of mesoscale convective systems and implications for large-scale heating. *Quart. J. Roy. Meteor. Soc.,* **115,** 425–461.

Iguchi, T., and R. Meneghini, 1994: Intercomparisons of single frequency methods of retrieving a vertical rain profile from airborne or spaceborne radar data. *J. Atmos. Oceanic Technol.,* **11,** 1507–1516.

——, T. Kozu, R. Meneghini, J. Awaka, and K. Okamoto, 2000: Rain profiling algorithm for the TRMM precipitation radar. *J. Appl. Meteor.,* **39,** 2038–2052.

Kawanishi, T., and Coauthors, 2000: TRMM precipitation radar. *Adv. Space Res.,* **25,** 969–972.

Kozu, T., and T. Iguchi, 1999: Nonuniform beam filling correction for spaceborne radar rainfall measurement: Implications from TOGA COARE radar data analysis. *J. Atmos. Oceanic Technol.,* **16,** 1722–1735.

——, and Coauthors, 2001: Development of precipitation radar onboard the Tropical Rainfall Measuring Mission (TRMM) satellite. *IEEE Trans. Geosci. Remote Sens.,* **39,** 102–116.

Kumagai, H., T. Kozu, M. Satake, H. Hanado, and K. Okamoto, 1995: Development of an active radar calibrator for the TRMM precipitation radar. *IEEE Trans. Geosci. Remote Sens.,* **33,** 1316–1318.

Kummerow, C., W. Barnes, T. Kozu, J. Shiue, and J. Simpson, 1998: The Tropical Rainfall Measuring Mission (TRMM) sensor package. *J. Atmos. Oceanic Technol.,* **15,** 809–817.

Meneghini, R., T. Iguchi, T. Kozu, L. Liao, K. Okamoto, J. A. Jones, and J. Kwiatkowski, 2000: Use of the surface reference technique for path attenuation estimates for the TRMM radar. *J. Appl. Meteor.,* **39,** 2053–2070.

——, J. A. Jones, T. Iguchi, K. Okamoto, and J. Kwiatkowski, 2001: Statistical methods of estimating average rainfall over large space–timescales using data from the TRMM precipitation radar. *J. Appl. Meteor.,* **40,** 568–585.

Pruppacher, H. R., and K. V. Beard, 1970: A wind tunnel investigation of the internal circulation and shape of water drops falling at terminal velocity in air. *Quart. J. Roy. Meteor. Soc.,* **96,** 247–256.

Ryzhkov, A., and D. S. Zrnic, 1995: Precipitation and attenuation measurements at a 10-cm wavelength. *J. Appl. Meteor.,* **34,** 2121–2134.

Schumacher, C., and R. A. Houze, 2000: Comparison of radar data from the TRMM satellite and Kwajalein ocean validation site. *J. Appl. Meteor.,* **39,** 2151–2164.

Simpson, J., C. Kummerow, W.-K. Tao, and R. F. Adler, 1996: On the Tropical Rainfall Measuring Mission (TRMM). *Meteor. Atmos. Phys.,* **60,** 19–36.

Steiner, M., R. A. Houze, and S. E. Yuter, 1995: Climatological characterization of three-dimensional storm structure from operational radar and rain gauge data. *J. Appl. Meteor.,* **34,** 1978–2007.

Tokay, A., and D. A. Short, 1996: Evidence of tropical raindrop spectra of the origin of rain from stratiform and convective clouds. *J. Appl. Meteor.,* **35,** 355–371.

Yuter, S. E., and R. A. Houze Jr., 1997: Measurements of raindrop size distributions over the Pacific warm pool and implications for *Z–R* relations. *J. Appl. Meteor.,* **36,** 847–867.